Science of the Total Environment 615 (2018) 240–252

Contents lists available at ScienceDirect

Science of the Total Environment

journal homepage: www.elsevier.com/locate/scitotenv

Beryllium-7 measurements of wind erosion on sloping fields in the wind-water erosion crisscross region on the Chinese Loess Plateau

Jiaqiong Zhang [a], Mingyi Yang [a,*], Xinxin Deng [a], Zhang Liu [b], Fengbao Zhang [a], Weiying Zhou [a]

[a] State Key Laboratory of Soil Erosion and Dryland Farming on the Loess Plateau, Institute of Soil and Water Conservation, Northwest A&F University, Yangling, Shaanxi 712100, China
[b] Rare Earth Research Institute of Baotou, Baotou, Inner Mongolia 014030, China

HIGHLIGHTS

- This study used beryllium-7 measurements to characterize wind erosion rates and their spatial distributions.
- Isolines revealed resultant effective erosion wind directions and variations in the microrelief.
- Wind erosion rates correlated better with linear slope gradients compared to the exponent.
- This study determined that beryllium-7 is feasible for wind erosion study in field experiments.

GRAPHICAL ABSTRACT

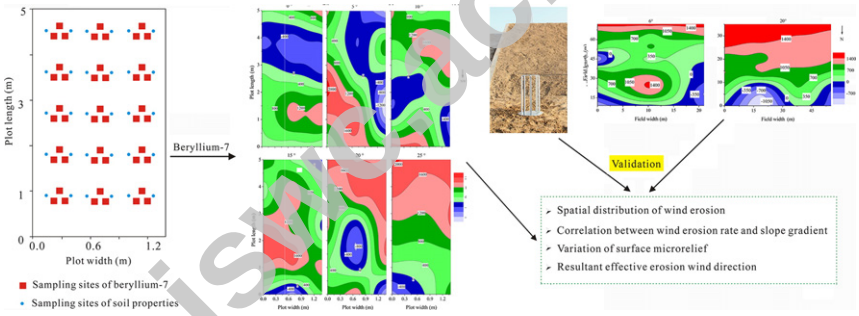

ARTICLE INFO

Article history:
Received 27 June 2017
Received in revised form 8 September 2017
Accepted 22 September 2017
Available online 29 September 2017

Editor: D. Barcelo

Keywords:
Beryllium-7 measurements
Resultant effective erosion wind direction
Slope gradient
Isoline distribution
Crisscross region

ABSTRACT

Soil erosion is complex in the wind-water erosion crisscross region of the Chinese Loess Plateau, as interleaving of wind and water erosion occurs on both temporal and spatial scales. It is difficult to distinguish wind erosion from the total erosion in previous studies due to the untraceable of aeolian particles and the limitation of feasible methods and techniques. This study used beryllium-7 measurements to study wind erosion in the wind-water erosion crisscross region on the Chinese Loess Plateau arms to delineate wind erosion distribution, to analyze its implication to erosive winds and surface microrelief, and to determine correlations between erosion rates and slope gradients. Results obtained using beryllium-7 measurements based on observation plots were verified with saltating particle collection method, and were also verified on a field scale. Results indicated that the effective resultant erosion wind was from northward, which was proved by the eight-directional distributed saltating particles. The microrelief of the ground surface contributed to the formation of high or low erosion centers. Wind erosion rates increased with a linear ($R^2 \geq 0.95$) or exponential ($R^2 \geq 0.83$) fitting increase in the slope gradients as reported in previous studies. Compared to wind erosion on field scale, both the plots and fields exhibited similar distribution patterns in wind erosion isolines. We also determined that the wind erosion rate for two fields estimated, based on equations developed from plot scale was acceptable. This study validates the feasibility of beryllium-7 measurements for soil-wind erosion field experiments and the potential to expand this approach to real field conditions.

1. Introduction

Soil-wind erosion, which widely occurs in arid and semiarid regions throughout the planet, contributes greatly to land degradation. Wind-driven emissions negatively affect soil texture, nutrient content, air

* Corresponding author at: No. 26 Xinong Street, Yangling, Shaanxi 712100, China.
E-mail address: ymyzly@163.com (M. Yang).

https://doi.org/10.1016/j.scitotenv.2017.09.238
0048-9697/

and water quality, human health, crop productivity, and sustainable land use in both local and geographically distributed areas (Larney et al., 1998; Lee et al., 1999; Wang et al., 2006; Warren, 2007). Soil erosion is severe on the Chinese Loess Plateau, where erosion rates are presently far beyond tolerable levels (Fu et al., 2011a). Furthermore, soil erosion in the wind-water erosion crisscross region is much more severe compared to other areas dominated by wind erosion (e.g., the northern area) or water erosion (e.g., the southern area) attributed to both vulnerable ecological environment and dramatic changes of climate. The vulnerable ecological environment is decided by the location of this region, it is a transition region between Mu Us Sandy lands and the Loess Plateau, having complicated soils and landforms, relatively sparse vegetation cover, and unreasonable land use. The dramatic changes of climate allows erosion occurring alternatively and accelerating mutually by wind and water. Thus, it has today become the most severely eroded region in China (Tang et al., 1993; Zhang et al., 2016). With the vast implementation of soil water conservation and ecological restoration projects in China throughout the past fifty or more years, the sediment loading of the Yellow River decreased from approximately 1.6 billion tons to 0.3 billion tons (Wang et al., 2007; Wang et al., 2016). Under this backdrop, the wind-water erosion crisscross region located in the high and coarse sediment region has still been subjected to serious erosion processes, and it has become a very important source area for sediment production, especially coarse particles that continue to be released to the lower reaches of the Yellow River (Liu et al., 2013; Zha and Tang, 2000). Furthermore, it is inherently difficult to study erosion processes in this region. The complex combination of the effects of wind and water erosion has resulted in limited available studies, which have produced conflicting results. This has been further complicated by the diversified underlying surface, which includes terrain, soils, land use patterns, and diverse vegetation (Du et al., 2016; Zhang, 1997; Zhao et al., 2017).

Terrain is a very important factor that affects soil erosion and sediment transport in hilly areas. In the past, slope gradients were believed to be the most important factor (Desmeta et al., 1999; Mahmoodabadi et al., 2014; Rahmati et al., 2017; Wu et al., 2016). However, previously published soil erosion research on slope gradients mostly concentrated on rain-induced erosion. Although results from previous studies on critical slope gradients of soil erosion and their influencing factors (Fu et al., 2011b; Ouchi, 2015; Vigiak et al., 2015) were able to established relationships between slope gradients and erosion rates, results have been inconsistent (Chaplot and Le Bissonnais, 2003; Mahmoodabadi and Sajjadi, 2016; Shen et al., 2016). Moreover, for those that analyzed the impacts of slope gradients on underlying surfaces (Ouchi, 2015; Ribolzi et al., 2011), even trace sediment sources have combined slope gradients with other parameters (Beauvais et al., 2007). With regard to studies on the effects of slope gradients on soil-wind erosion, they have mostly focused on variations in near-surface sand transport, wind velocity thresholds, erosion rates, and patterns of aeolian activity in arid regions, primarily using sand dunes as objects of study (Atwood-Stone and McEwen, 2013; Faria et al., 2011; Iversen and Rasmussen, 1999; Sun and Huang, 2017). Some studies found that soil-wind erosion was exponentially related to slope gradients (Hong et al., 2014), while other studies found no direct relationship between wind erosion and slope gradients but a significant negative relationship between changes in erosion intensity and slope gradients (Zhou et al., 2015). Moreover, wind erosion has increased with increasing slope gradients, and, depending on soil type, its trend in variation will change at a critical slope gradient (Hong et al., 2014; He et al., 2013). In regions outside strong aeolian activity, only limited studies have taken into account soil-wind erosion on sloping fields, and almost all only pertained to low, gentle slopes (Fryrear et al., 1998; USDA, 1996). That is to say, barely any studies have been conducted on wind erosion in regions affected by multi-erosion forces, such as the wind-water erosion crisscross region of the Chinese Loess Plateau.

However, the greatest obstacle is the interaction between wind and water erosion, making it difficult to distinguish between contributions of wind erosion out of the total erosion that takes place. Before recent technical advances in erosion measurements, researchers studied wind erosion by tracking changes in soil surfaces or analyzing particulate matter collected from the atmosphere (Hagen et al., 2010; Offer and Goossens, 1995). Water erosion was typically studied by measuring sediment and runoff (Zhang et al., 2011); wind and water erosion were normally measured using different techniques independently. Consequently, such techniques were inadequate owing to the complexity of the task. Experiments that combined wind tunnels and simulated rainfall basically divided wind and water erosion into separate constituents (Tuo et al., 2016; Zhang et al., 2016). These earlier techniques were basically simplified unidirectional processes given that the direction of wind and water on slope gradients were not taken into account. In fact, for windward slopes strongly impacted by wind erosion, the direction of wind is from the toe to the top of the slope, while the direction of water is downward in what is essentially the opposite direction. In addition, the influence of slope gradient on wind erosion is beyond the capacity of laboratory simulations. Thus, on-site investigations based on a feasible technique is clearly a more rational approach to take.

Beryllium-7 is a suitable radionuclide to study the effects of wind erosion in crisscross regions owing to its short half-life (53.5 d), continual deposition, generally decreasing exponentially increasing soil depth, and high sensitivity in the topsoil profile (Blake et al., 1999; Yang et al., 2006). Its short half-life makes it impossible for it to be transported into the deeper soil layers, and it possesses unique advantages in tracing short-term soil processes (Landis et al., 2016; Walling et al., 1999; Yang et al., 2013). Furthermore, the high concentration of beryllium-7 in topsoil, especially in surface soil, makes it sensitive to even slight soil erosion, that is, the removal of a thin layer of soil will generally result in a significant change in the beryllium-7 inventory. Therefore, it is an effective and easy approach to obtain accurate erosion rates. On the Chinese Loess Plateau, beryllium-7 is distributed within the 0–20 mm soil layer and is concentrated within the 0–2 mm soil layer (Yang et al., 2006). Beryllium-7, therefore, is a reliable approach to use for soil water erosion research (Zhang et al., 2013, 2014). Beryllium-7 content in soil is influenced by factors that include soil properties, seasons, latitude, vegetation, and precipitation (Ayub et al., 2012; Wallbrink and Muruay, 1996). Deposition of beryllium-7 is primarily through wet deposition processes (Wallbrink and Muruay, 1996). On the Chinese Loess Plateau, beryllium-7 deposited mainly during the rainy season (June and September), where barely any rainfall-driven erosion occurs after October. This provides sufficient time for the stabilization of beryllium-7 in the soil profile during the windy season, for which rainfall erosion would had basically no impact. Moreover, during winter, vegetation has little effect on the deposition of beryllium-7 on the bare ground surface (Zhang et al., 2011), which improves wind erosion rate estimation accuracy. It is therefore beryllium-7 should be an optimal choice for tracing soil-wind erosion processes on the Chinese Loess Plateau. Besides, a study by Yang et al. (2013) approved its feasibility in wind erosion study through wind tunnel experiments.

This study assumed that beryllium-7 could be used to distinguish wind erosion from the total erosion when wind erosion and water erosion occurs alternately. This means that the activity of beryllium-7 in soil is delectable at the end of the windy season, and rainfall erosion occurred scarcely after the setting of experiments. We investigated wind erosion rates on a plot scale under different slope gradients based on the beryllium-7 approach in a watershed within the wind-water erosion crisscross region on the Chinese Loess Plateau. The objectives of this study were to describe the spatial distribution of wind erosion on sloping cropland, to analyze the implication of erosion isolines to effective erosion winds and surface microreliefs, and to determine the relationships between wind erosion rates and slope gradients. Results were verified through observation of saltating particle discharge on plots, and soil wind erosion estimation on a field scale.

2. Materials and methods

2.1. Study area

This study selected the Liudaogou watershed as the experimental site (38°46′–38°51′ N, 110°21′–110°23′ E), which is located 14 km west of Shenmu County in Shaanxi Province, China (Fig. 1). The average elevation of the watershed ranges from 1273.9 m to 1081.0 m AMSL from northwest to southeast. The highly fragmented loess hills, with a gully channel density of 7.4 km km^{-2}, have both aeolian and fluvial geomorphologic characteristics. The local weather is characterized by dramatic interannual variations. According to records from 1957 to 2011, the average annual temperature is 8.9 °C, with a maximum average of 25.0 °C in July and a minimum average of −8.1 °C in January. Temperature was approximately zero in November (averaged 1.1 °C) and below zero in December, January and February. Annual precipitation averages 422.7 mm, most of which (76.3%) falls as rainfall from June through September (Wu, 2013). The prevailing wind direction is from the northwest, and the annual average wind velocity is 3.6 m s^{-1}. There are 13.5 annual average gale days. Frequent episodes of blowing sand also occur (approximately 255.1 h per year), most of which (63.0%) take place in April. Local vegetation is sparse in the region, and sloping cropland is widely distributed. The lack of ground cover allows for extensive water and wind erosion to occur throughout the year, which is due to alternating strong winds and heavy rainfall. The soil in the region is dominated by silt loam and sandy loam. Aeolian sand also appears patchy or in sheets, which is based on the texture-based classification by the United States Department of Agriculture (USDA, 1951).

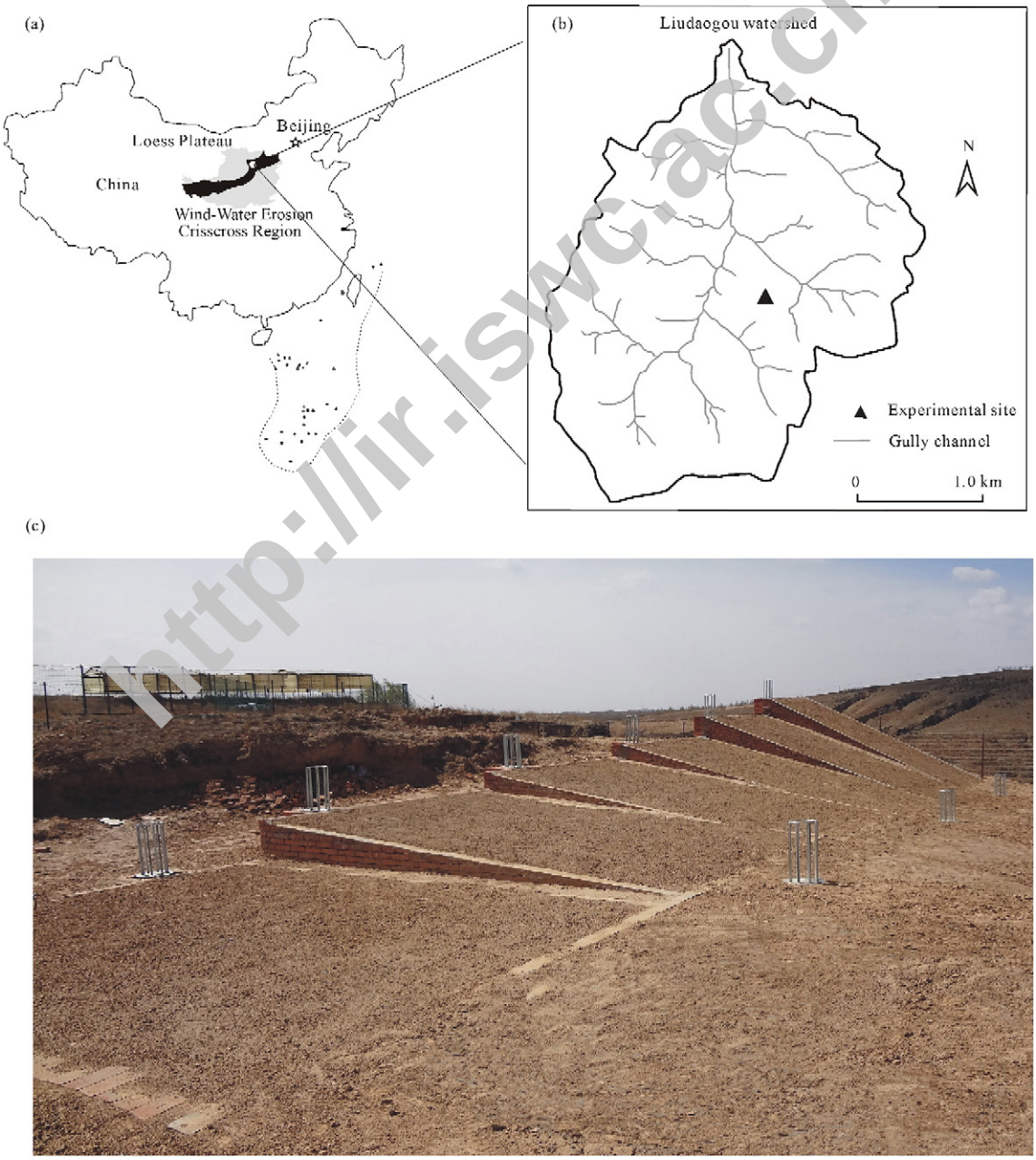

Fig. 1. Location of the study area, the wind erosion investigation plots, and the sand sampler mounts.

2.2. Experimental design and soil sampling

In the Liudaogou watershed, this study established wind erosion plots (1.4 × 5 m) of six different gradients (0°, 5°, 10°, 15°, 20°, and 25°) in the upper area of northwest-facing slopes. After the rainy season (at the beginning of October), we smoothed the fields and mounted the sand samplers at both downwind positions of all plots and upwind positions of the plots at slope gradients of 5°, 15°, and 25°. Each sand sampler had eight openings facing eight primary directions. The width of openings were 5 mm, and the collection height was 50 cm (Fig. 1). Opening locations on these 27 cm diameter circles all faced outward. At the same time, this study established two beryllium-7 reference plots (one near the plots and the other near the sampling fields) at positions least affected by wind. At the end of the windy season (in the middle of May), we collected two types of samples from the plots. One group was used to test beryllium-7 activity. We collected each sample from the 0 to 2.5 cm surface layer with a 10 × 10 × 2.5 cm square sampler three separate times to provide approximately 500 g of samples for tests. Moreover, we collected 15 samples from each plot with a grid distribution of five lines. We collected the other group of samples from the crust layer (from approximately 0 to 0.5 cm) and from 1 to 2 cm on two occasions using a core sampler with an internal diameter of 3 cm adjacent to each beryllium-7 sample. These samples were used to analyze grain size and specific surface area (SSA). In total, we collected 30 samples from each plot (Fig. 2). Two reference plots (2 × 2 m) were enclosed with 1 m tall walls on the leeward slopes of flat grassland. For each beryllium-7 reference plot, we collected five bulk samples at a 0 to 2.5 cm depth using a 10 × 10 cm square sampler, and we collected a group of incremental depth samples using a purpose-designed depth-incremental scraper plate sampling device with a diameter of 10.5 cm. Soil cores were extracted using a threaded rod, and residual soil was removed by a scraper blade. Moreover, we collected soil at a 2.5 cm depth in 10 layers with a depth-increment of 2.5 mm in a 60 × 60 cm area. Finally, we collected a total of 72 saltating particles from nine sand samplers. At the same time, we collected two sloping cropland samples from the upper areas of the north-facing slope. The size of the fields were approximately 55 × 35 m and 72 × 21 m, respectively. The slope gradients of fields were approximately 6° and 20°, respectively. These fields possessed the same soil type as the observation plots. They were plowed, smoothed, and left bare after harvest. The sampling approach we used for soil samples was the same as for the plots. There were three transects with six sampling sites on each line for the 6° field, and three transects with eight sampling sites on each line for the 20° field. The sample types and numbers were summarized in Table 1. Besides, rainfall was recorded using a RG3-M tipping bucket rain gauge (Onset Computer Corporation, MA, USA) located on the flat hilltop approximately 20 m southeast of the study plots. We conducted these investigations during two windy seasons from October 2014 to May 2016.

For the beryllium-7 tests, a total of 240 soil samples from six plots and 42 soil samples from two bare sloping croplands were air-dried, ground, passed through 1 mm sieve, and weighed prior to analysis. We determined beryllium-7 activity (Bq kg^{-1}) using a gamma spectrometry with a low background measurement hyperpure coaxial germanium detector coupled to a multichannel analyzer system (EG&G ORTEC, Oak Ridge, USA). We conducted measurements at 477.6 keV with an approximate count time of 86,400 s. The detector was calibrated prior to tests using a certified multi-radionuclide standard of a known activity (supplied by the China Institute of Atomic Energy (CIAE), including: U-238, ±2.2%; Th-232, ±2.7%; Ra-226, ±3.2%; Pb-210, ±2.9%; K-40, ±2.7%; Cs-137, ±0.4%, and Co-60, ±0.2%). The precision of beryllium-7 activity was from ±5% to 6% at a 95% confidence level. For all soil samples, we converted measured beryllium-7 activity to values at the sampling time using an appropriate decay constant. The 364 samples for the grain size and SSA tests were first air-dried, ground, and passed through 2 mm sieve before organic matter and calcium carbonate were removed prior to testing using the Mastersizer 2000 (Malvern Instruments, Malvern, UK). We removed saltating particle impurities, such as grass and insects, prior to establishing weight, and we measured grain size using the S-4800 Cold Field-Emission Scanning Electron Microscope (Hitachi High-Technologies Co. Ltd., Shenzhen, Guangdong Province, China). Pictures obtained were analyzed using an image-Pro Plus 6.0 analysis system (Media Cybernetics, Inc., Shanghai, China). We analyzed eight pictures from each sample and averaged them per grain size. The mean grain size and standard deviation of the samples were calculated using Folk and Ward's formulas (Folk and Ward, 1957). The grain size was divided into clay (<0.002 mm), silt (from 0.002 to 0.050 mm), very fine sand (from 0.05 to 0.1 mm), fine sand (from 0.1 to 0.25 mm), medium sand (from 0.25 to 0.50 mm), coarse sand (from 0.5 to 2.0 mm), and gravel (>2.0 mm) based on the grading standard used by the USDA (1951).

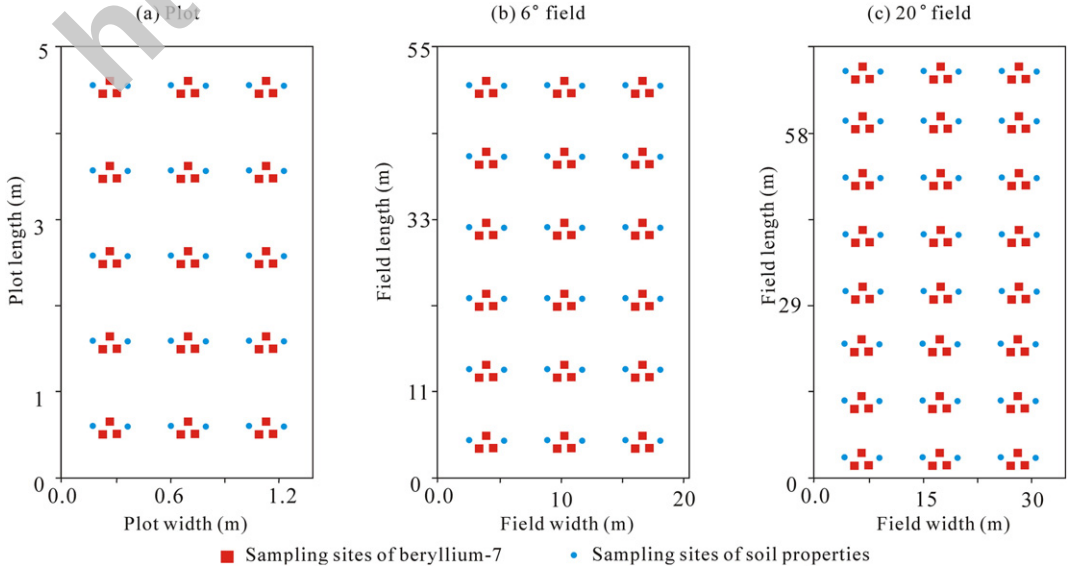

Fig. 2. Distribution of sampling sites for plots (a) and fields (b,c).

Table 1
Summary of sampling types and numbers.

Sampling area	Number of sampling area	Type of samples		
		Beryllium-7	SSA	Saltating particles
Plot (0°–25°)	12	15	30	8
Field (6°)	1	18	36	0
Field (20°)	1	24	48	0
Depth-incremental reference	2	10	0	0
Bulk reference	2	5	0	0

2.3. Estimation of soil-wind erosion rates

Based on wind tunnel experiments, Yang et al. (2013) developed a wind erosion estimation model for beryllium-7 measurements by comparing differences in the beryllium-7 inventory between reference sites and tested plots. The results of the model were verified by the saltating particle collection method and applied to the Liudaogou watershed.

For locations where wind erosion has taken place, the erosion rate R_{Be} (kg m^{-2}) was estimated using the following equations:

$$R_{Be} = P' h_0 \left(\frac{A_{ref}}{A_{Be}}\right) \quad (1)$$

$$P' = \left(\frac{S_e}{S_o}\right)^{v} \quad (2)$$

where P' is the particle size correction factor for wind erosion; h_0 is the relaxation mass depth (kg m^{-2}); A_{ref} is the inventory of beryllium-7 at the reference site (Bq m^{-2}); A_{Be} is the measured total inventory of beryllium-7 at the eroded site (Bq m^{-2}); S_e is the SSA of surface soil after wind erosion; S_o is the SSA of the original surface soil before wind erosion, which was replaced with the SSA of soil samples collected form 1 to 2 cm depth; and v is a constant. In this study, we used 0.75 as the constant *ca* as reported by Yang et al. (2013).

The beryllium-7 inventory will increase at locations of wind deposition, and the depositional rate R'_{Be} (kg m^{-2}) was estimated using the following equation:

$$R'_{Be} = \frac{A_{Be} - A_{ref}}{P' C_{Be,d}} \quad (3)$$

Depending on the declining exponent distribution of beryllium-7 in the soil profile, we calculated the mean beryllium-7 activity in deposited sediment $C_{Be,d}$ (Bq kg^{-1}) using the model provided by Walling et al. (1999) as follows:

$$C_{Be}(x) = \frac{\int_s C_{Be,e} R_{Be} ds}{\int_s R_{Be} ds} \quad (4)$$

$$C_{Be,e} = A_{ref}\left(1 - e^{-\frac{R_{Be}}{h_0}}\right)/R_{Be} \quad (5)$$

where x is the mass depth from the soil surface (kg m^{-2}); $C_{Be}(x)$ is the concentration of beryllium-7 at depth x (Bq kg^{-1}); and $C_{Be}(0)$ is the mass activity density of the surface soil (when x is 0) (Bq kg^{-1}).

3. Results

3.1. Depth distribution of beryllium-7 and its reference inventory

Soil type was silt loam in this study (Table 2). The activity of beryllium-7 was detectable for almost all samples (five undetectable samples in 2015 for plots). It ranged from 74.75 Bq m^{-2} to 420.15 Bq m^{-2}, averaged 196.88 Bq m^{-2} in 2015; and ranged from 92.78 Bq m^{-2} to 486.76 Bq m^{-2}, averaged 199.03 Bq m^{-2} in 2016 (Table 3). Beryllium-7 was distributed as exponential functions within the shallow soil depth at a concentration from 0 to 2 mm (Fig. 3). This indicated that the measured beryllium-7 distribution in the soil profile provided a good fit to wind-driven soil loss estimations. Mass depths during the 2015 and 2016 windy seasons were 2.05 kg m^{-2} and 2.13 kg m^{-2}, respectively. Thus, the exponential relationship between areal activity density (A_{Be}; Bq m^{-2}) of beryllium-7 and the mass depth (x; kg m^{-2}) during the 2015 and 2016 windy seasons were respectively as follows:

$$A_{Be}(x) = 221.0e^{-x/2.05} (n) = 5,\ R^2 = 0.96 \quad (5)$$

$$A_{Be}(x) = 240.93e^{-x/2.13} \left(n = 5,\ R^2 = 0.95\right) \quad (6)$$

For the measured reference samples, the mean inventory was 223.48 ± 12.56 Bq m^{-2} and 250.47 ± 13.65 Bq m^{-2} in 2015 and 2016, respectively. When taking the sampling variability, soil heterogeneity, and measurement precision limitations (approximately from ±5% to 6% at a 95% confidence level) into consideration, this study averaged the theoretical values and 10 reference cores as the final reference inventory for soil loss estimations, which were 222.80 Bq m^{-2} and 246.66 Bq m^{-2} in 2015 and 2016, respectively.

Table 2
Silt loam soil properties.

	Mean grain size (mm)	Sorting (Φ)	Clay (%)	Silt (%)	Very fine sand (%)	Fine sand (%)	Medium sand (%)	Coarse sand (%)
2015	39.52 ± 2.07	2.10 ± 0.04	12.38 ± 0.95	57.31 ± 1.87	21.21 ± 1.19	8.98 ± 1.18	0.12 ± 0.25	0.005 ± 0.03
2016	37.64 ± 3.75	2.05 ± 0.08	12.15 ± 2.24	19.85 ± 3.47	20.34 ± 2.12	7.37 ± 1.93	0.26 ± 0.37	0.007 ± 0.09

Table 3
Beryllium-7 (Bq m^{-2}) activity for observation plots within the sampling sites.

	0°	5°	10°	15°	20°	25°
2015	181.43 ± 29.82	171.46 ± 28.78	207.29 ± 34.65	190.61 ± 29.55	230.11 ± 26.08	200.39 ± 28.70
2016	223.91 ± 22.76	197.10 ± 25.52	173.53 ± 27.42	193.16 ± 26.39	185.65 ± 25.96	220.80 ± 24.75

Uncertainty at a 95% level of confidence.
Uncertainty was calculated using the net area (A) of ^{137}Cs activity (Owens et al., 1996) as follows: $M_e = 1.96 \times 100(\frac{\sqrt{A}}{A})$.

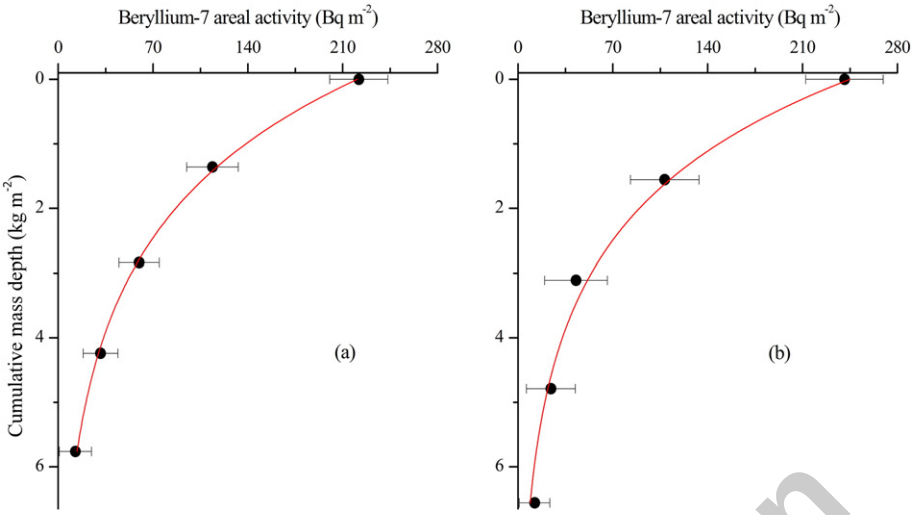

Fig. 3. The depth distribution of beryllium-7 at the reference site in 2015 (a) and 2016 (b).

3.2. Wind erosion rate distribution based on beryllium-7 measurements

The rainfall data in the windy season during study periods showed that rainfall erosion barely occur during the study periods (Table 4). Based on reference and sampling site inventories of beryllium-7 (Table 3; Figs. A1 and A2), we estimated the wind erosion rate. Beryllium-7 measurements on plots with different slope gradients provided the soil distributions (Fig. 4 and Fig. 5). Wind erosion ranged from -1438.6 t km^{-2} (a negative value represented wind deposition) to 2177.7 t km^{-2} during the two year observational periods and averaged 587.9 t km^{-2} regardless of the slope gradient of plots. Isolines of soil loss varied significantly both from plots to plots and from year to year. However, common patterns included the following three specific aspects. Firstly, there were areas that isolines bent and formed high or low erosion centers. The surface microrelief was the cause of this variation, and isoline bending directions provided the evidence. Convex areas showed greater erosion rates and increased wind erosion rates for certain positions in upwind areas, and vice versa for concave areas. In this respect, the shape of erosion isolines could be used to determine the surface microrelief during erosion processes. Secondly, the straight isolines angled with plot direction, which was almost perpendicular to northern direction with the exception of the flat plot (0°). For the flat plot, isolines were perpendicular to the northwest being affected by a low convex landform on its northeastern side as shown by investigation. The normal variation of isolines indicated that the resultant effective erosion wind direction for erosion was from the north. In this respect, the direction of straight erosion isolines could be used to determine the resultant effective force of wind erosion. Thirdly, wind erosion rates were greater at downwind positions of the slope for most plots, and deposition was observed in all plots, especially at upwind positions. The distributed deposition may be caused by soil packing of the plots. It was practically impossible to smooth the ground totally flat. These wind-driven soil loss distribution patterns implied that beryllium-7 measurements could visualize the wind erosion distribution that was found to be too difficult to track in previous studies. Therefore, this method would be very useful for wind erosion studies.

3.3. Variation in the wind erosion rates with slope gradients

Wind erosion rates increased with increasing slope gradients in bare ground plots in this study. Its increasing rate was much lower from 20° to 25°(with a two year average of 28.3 t km^{-2}) compared to lower slope gradients (>81.8 t km^{-2}). This indicated that 20° was a turning gradient for the variation of erosion by wind, and the critical erosion gradient was not lower than 25°. Variation in wind-driven erosion rates corresponded well with both the linear function ($E = a\theta + b$; a and b were constants) ($R^2 \geq 0.95$) and the exponential function ($E = ce^{d\theta}$; c and d were constants) ($R^2 \geq 0.83$), and linear fitting was determined to be better than exponential fitting. Based on the 2015 and 2016 correlative equations and their averages, the constant "a" was approximately 22, "b" was close to "c", and "d" ranged from 0.04 to 0.06 (Table 5). Unfortunately, current data did not provide sufficient information to affirm constant "b" and "c". Hong et al. (2014), taking multiple factors into account, observed exponential relationships between slope gradients and wind erosion rates using a portable wind tunnel. He et al. (2013) observed an increasing to decreasing soil erosion rate at an approximate 20° gradient for loam soil using wind tunnel experiments. The soil erosion rate fitted linear ($R^2 \geq 0.95$) or exponential ($R^2 \geq 0.95$) functions before decreasing at tested wind velocities (Table 5).

Table 4
Rainfall condition during windy seasons (mm).

Duration	Total rainfall	Monthly maximum	Daily maximum	Hourly maximum	Maximum of single event rainfall*		
					Rainfall	Duration (h)	Date
10/2014–5/2015	100.6	28.2 (April)	13.0	5.6	13.0	7	10/1
10/2015–5/2016	146.2	65.2 (November)	35.6	4.4	25.4	15	11/5

The precipitation in the form of snow was not included.
* Single rainfall event rainfall was hours that rainfall continuous regardless of natural day.

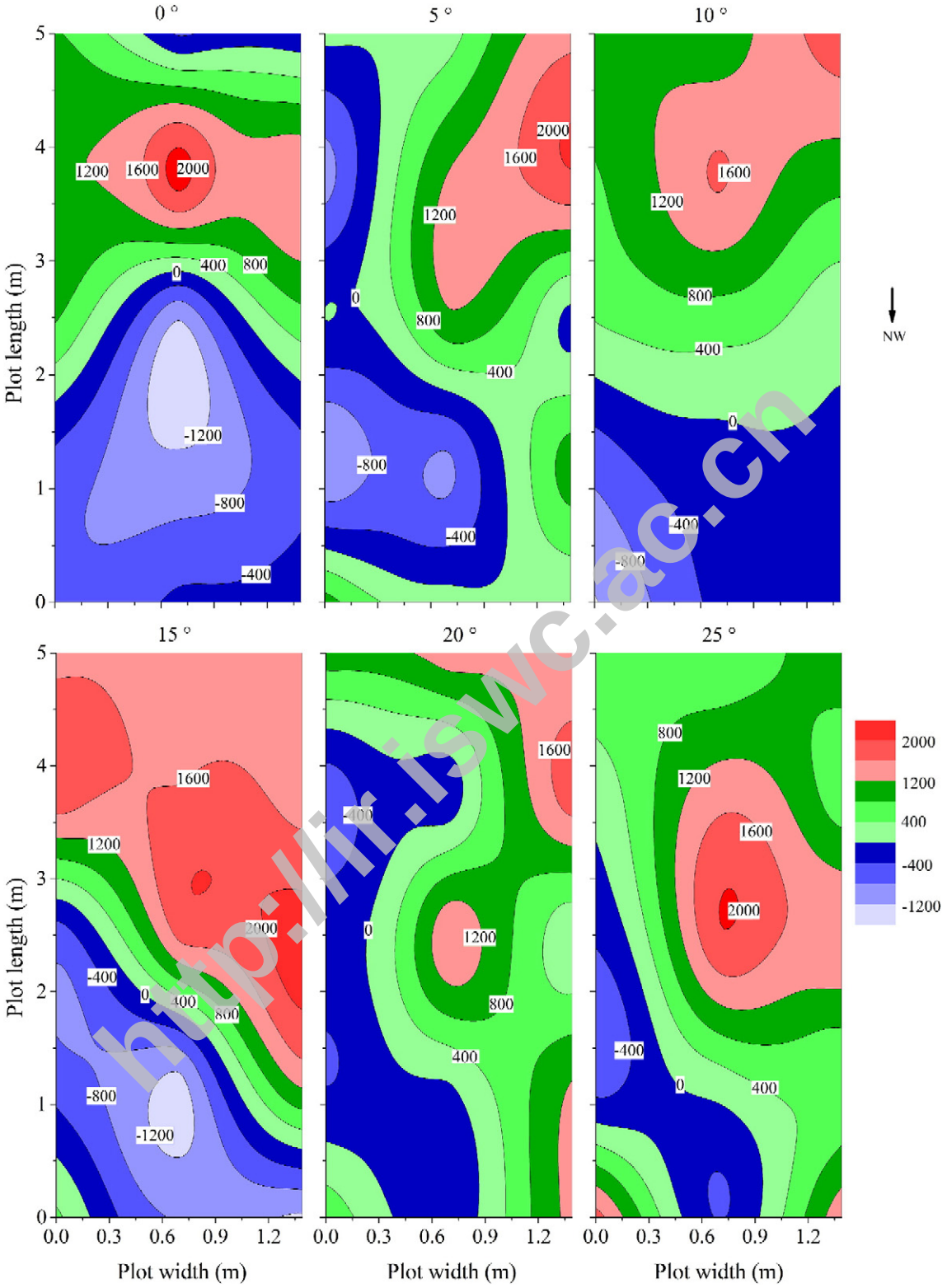

Fig. 4. The distribution of soil loss by wind in plots during the 2015 windy season.

3.4. Saltating particle distribution in eight primary directions

Saltating particle distribution in all eight directions exhibited similar patterns during the two year of observation. On average, the northern direction yielded the maximum value, and followed by the northwestern direction. The southern and southeastern directions yielded the minimum values, with the exception of the 0° plot. For the 0° plot, the northwestern direction yielded the greatest amount of eroded saltating

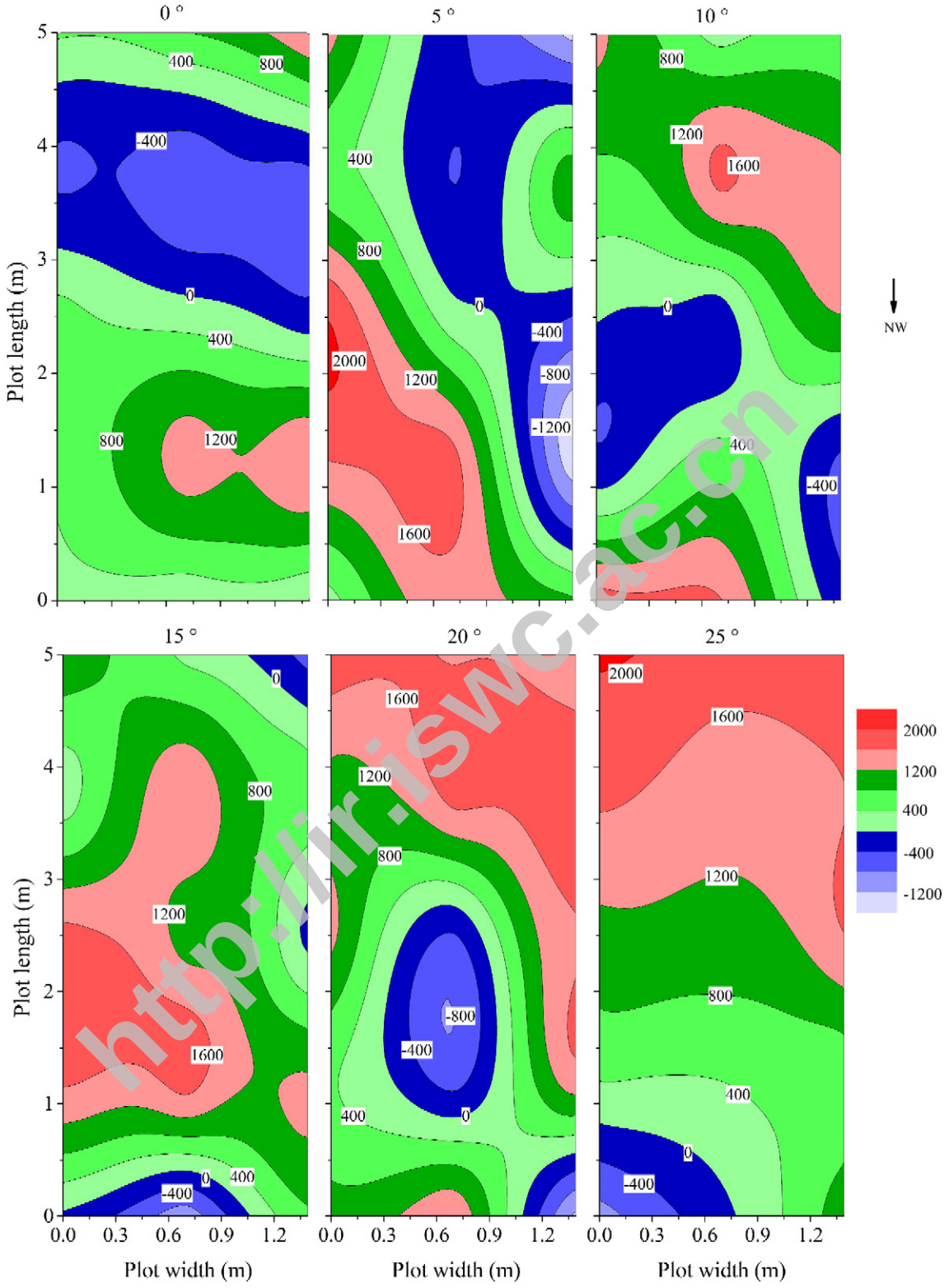

Fig. 5. The distribution of soil loss by wind in plots during the 2016 windy season.

particles, and followed by the northern direction. Compared to the other plots, the northeastern direction yielded a greater amount of saltating particles (Fig. 6).

Based on the local prevailing wind direction (northwest) and the direction of plots, winds from the northwest (NW), north (N), and west (W) transported soil upwind through the plots to their downwind positions, while winds from the southeast (SE), south (S), and east (E) transported soil downwind through the plots to their upwind positions. Thus, saltating particle collection from these directions for both upwind and downwind positions of the plots revealed the net

Table 5
Relationship between the wind erosion rate (E; t km^{-2}) and the slope gradient (θ; °).[a]

		0°	5°	10°	15°	20°	25°	30°	Correlative equation
This study	2015	141.1	341.4	458.0	571.0	674.9	695.7	—	$E = 22.21\theta + 202.73$, $R^2 = 0.95$ $E = 204.60e^{0.060\theta}$, $R^2 = 0.83$
	2016	287.0	466.8	609.4	691.1	811.2	847.1	—	$E = 22.37\theta + 339.07$, $R^2 = 0.96$ $E = 347.94e^{0.041\theta}$, $R^2 = 0.89$
	Average	214.1	404.1	533.7	631.1	743.1	771.4	—	$E = 22.29\theta + 270.92$, $R^2 = 0.96$ $E = 277.36e^{0.048\theta}$, $R^2 = 0.86$
He et al. (2013)[a]	8 m s^{-1}	72.7	75.8	119.9	—	188.6	—	118.3	$E = 6.18\theta + 60.18$, $R^2 = 0.95$ $E = 67.49e^{0.051\theta}$, $R^2 = 0.95$
	10 m s^{-1}	104.6	161.6	229.0	—	346.6	—	214.0	$E = 12.18\theta + 103.85$, $R^2 = 0.99$ $E = 114.56e^{0.059\theta}$, $R^2 = 0.97$

[a] The erosion rate from He et al. (2013) was determined by minute-averaged values (t km^{-2} min^{-1}).

soil loss from the plots (locations of sand collectors are provided in Fig. 1). The transport of soil from upwind to downwind direction was 205.5 g m^{-1}, 395.9 g m^{-1}, and 489.3 g m^{-1} for the plots with slope gradients of 5°, 15°, and 25°, respectively, and from downwind to upwind direction was 149.0 g m^{-1}, 184.8 g m^{-1}, and 173.0 g m^{-1}, respectively. The net transport of soil was from the upwind to the downwind positions of plots, and the net sediment discharge for the 5°, 15°, and 25° plots was 56.5 g m^{-1}, 211.1 g m^{-1}, and 316.3 g m^{-1}, respectively (Table 6). This also revealed an increase in soil-wind erosion in conjunction with increasing slope gradients. At the same time, soil transport in southwest (SW) and northeast (NE) directions was perpendicular to the direction of the plots, which may influence wind erosion among plots.

Mean grain sizes of the saltating particles collected ranged from 52.3 to 95.3 mm. The northern direction had the coarsest grain size (with an average of 89.4 mm for all plots), followed by the northwestern (73.4 mm) and the southern directions (70.4 mm) (Fig. 7). Sorting ranged from 0.33 Φ to 0.71 Φ with an average of 0.46 Φ. There was significant sorting differences ($P < 0.05$) in different directions for saltating particles collected downwind of the plots regardless of the plot gradient. The sorting of particles collected in the SW direction was significantly different compared to the NW and SW directions based on a pairwise comparison of one-way ANOVA in SPSS 19. The collected saltating particles from all observed directions were mostly dominated by very fine sand and the remaining by silt, while a small amount of the rest sizes was also found. Its variation was similar to that of grain

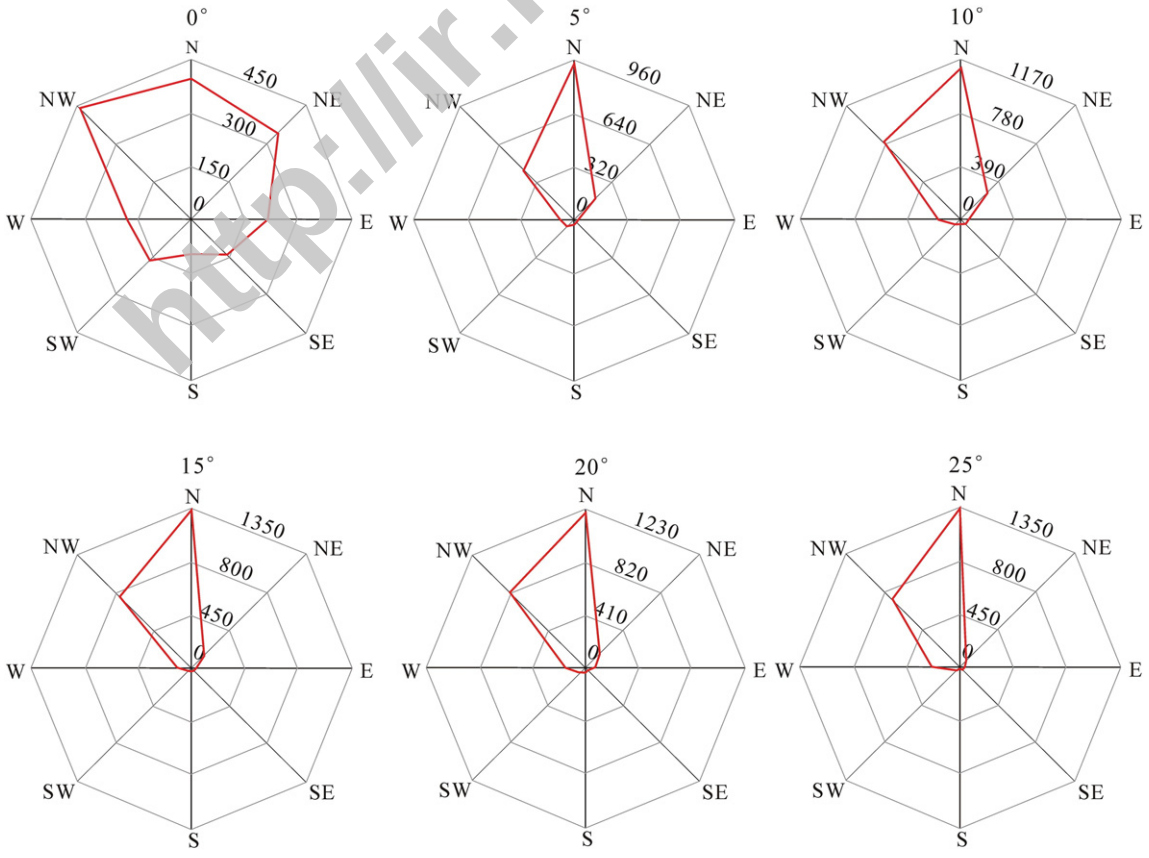

Fig. 6. Saltating particle transport (g m^{-1}) (from 0 to 50 cm) at the downwind position of each plot.

Table 6
Saltating particle transport (g m^{-1}) from plots with slope gradients of 5°, 15°, and 25°.

Plot	Location	NW[a]	N[a]	NE	E	SE	S	SW	W*
5°	Upwind	277.1	420.7	282.6	182	184.5	148.3	187.7	146.9
	Downwind	422.8	937.7	180.0	29.4	15.6	22.8	58.0	100.6
	Net transport	145.7	517.0	102.6	152.6	168.9	125.5	129.7	−46.3
15°	Upwind	380.8	583.7	408.7	188.8	193.8	245.3	176.0	189.9
	Downwind	875.3	1337.7	137.2	26.5	26.4	20.6	48.7	129.0
	Net transport	494.5	754.0	271.5	162.3	167.4	224.7	127.3	−60.9
25°	Upwind	308.5	371.1	391.2	215.9	211.4	148.0	211.4	192.7
	Downwind	837.7	1340.1	94.3	21.4	15.7	19.2	30.6	162.4
	Net transport	529.2	969.0	296.9	194.5	195.7	128.8	180.8	−30.3

Data reported in this table were the 2015 and 2016 averages.
[a] The net transport (g m^{-1}) was calculated using downwind values (g m^{-1}) subtracted by upwind values (g m^{-1}) for the NW, N, and W, as well as using upwind values subtracted by downwind values for the remaining directions.

size, which was coarsest in the northern direction (with an average of 74.9% for all plots), followed by the northwest (63.9%) and the southwest directions (59.4%) (Fig. 8). Distribution amounts of particle transport, grain-size, and content of very fine sand of saltating particles also indicated that northern and northwestern winds had a stronger erosion capacity than winds from other directions; moreover, the effective erosion energy of northern winds was stronger than northwestern winds.

4. Discussion

Given that eroded particles could be transported by wind in any direction, wind erosion in neighboring plots should experience interaction effects. Saltating particle collection in eight directions both upwind and downwind of the plots helped to make clear the influence degree of wind erosion rates between the plots. Differences in soil transport in opposite direction (SW–NE) perpendicular to the direction of plots would result in an associative influence between the two adjacent plots, while aeolian transport on opposite directional groups N–S and W–E had limited influence on the soil erosion rate of other plots. The net particle transport was from NE to SW, which means that eroded soil will be transported from the flank of the 5° plot to the 25° plot. The average transport of saltating particles from NE to SW was 15.5 g m^{-1}, which was the minimum value for all opposite directional groups (Table 7). Depending on the height differences of the plot boundaries (brick walls), aeolian transport from the 5° plot to the 25° plot increased in height, which would decrease the probability that eroded particles would be removed from lower slope gradient plots up to plots with higher slope gradients where they would then be deposited.

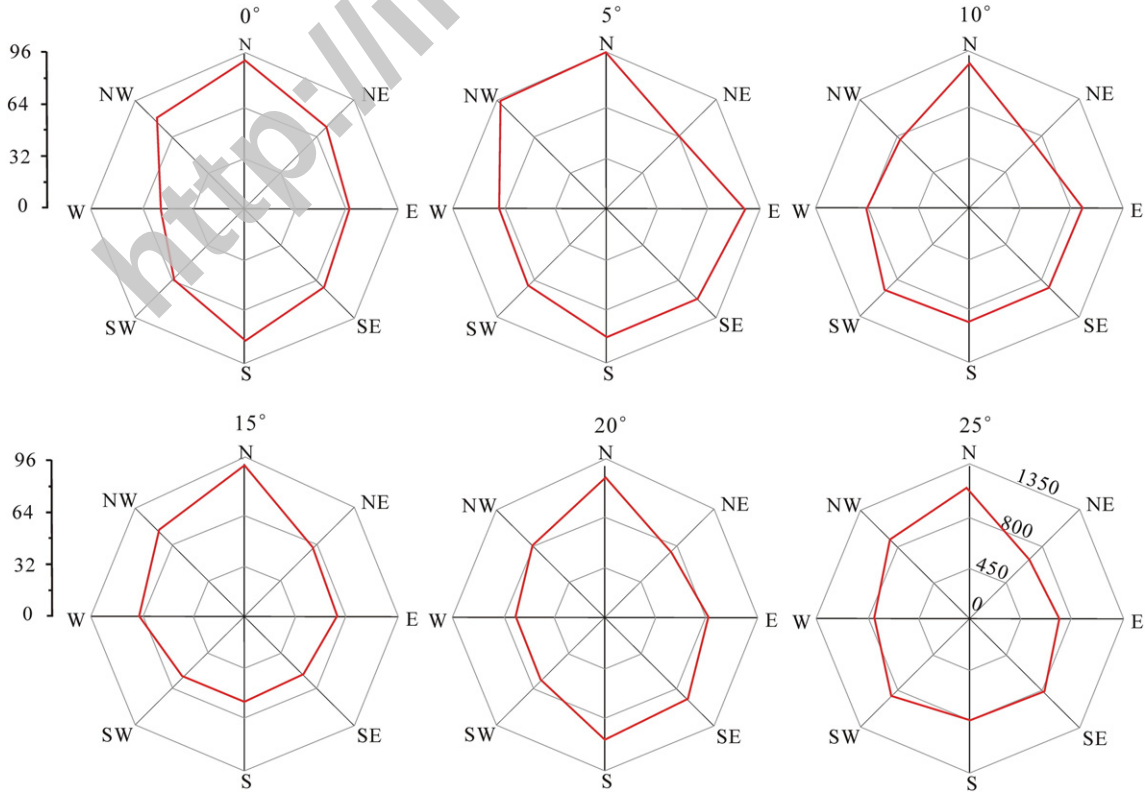

Fig. 7. Grain-size distribution of saltating particles in the downwind position of each plot.

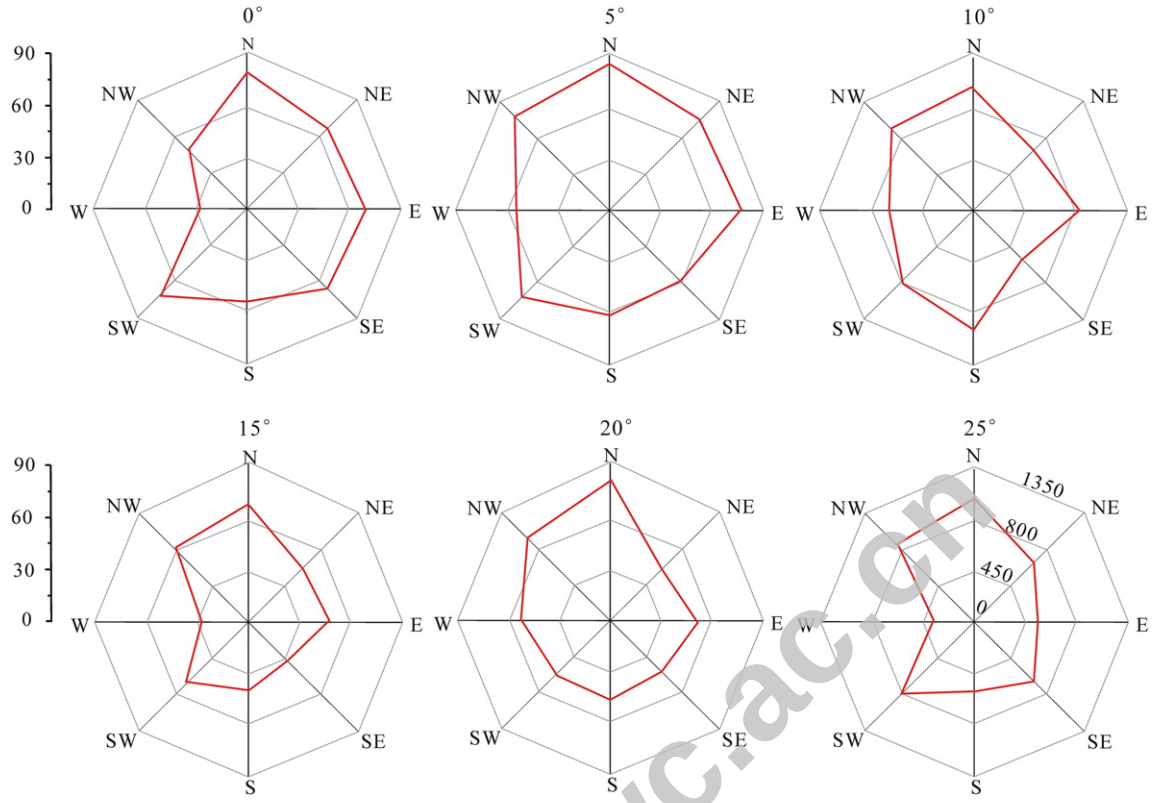

Fig. 8. The content of very fine sand in collected saltating particles in the downwind position of each plot.

In order to verify the real representation of wind erosion distribution on adjacent plots to wind erosion distribution in local sloping fields, this study investigated wind erosion from two north-facing bare sloping fields using beryllium-7 measurements. Results showed that wind erosion isolines were almost perpendicular to northern direction. The isolines bended in some areas and formed high or low erosion centers (Fig. 9). Deposition was mostly distributed in areas close to the upwind border of the field, which could be caused by differences in surface ground conditions. The upwind position (downslope area) of the crop field investigated was comprised of grassland with artificial shrubs (*Caragana korshinskii*) with an average height of 1.5 m. Vegetation almost fully covered the ground, which greatly increased the stability of the surface, and decreasing erosion energy on their downwind boundary (i.e., the upwind area of the crop field) (Al-Amin et al., 2010; Leenders et al., 2011). Thus, protection from the upwind area decreased wind-driven soil loss and even caused deposition in areas close to the upwind border. The similarity of isolines on both a field scale and a plot scale indicated that aeolian transport between plots was limited.

Table 7
Particle transport (g m^{-1}) in opposite directions.

Plot	N–S	NW–SE	W–E	SW–NE
5°	78.3	−4.6	−39.8	5.4
15°	105.9	65.4	−44.6	−28.8
25°	168.0	66.7	−45.0	−23.2
Average	117.4	42.5	−43.1	−15.5

Data reported in this table were the 2015 and 2016 averages. They were calculated based on the net transport of particles on each direction.
Results in this table were the net directional particle transport from the direction before the "–" to the direction after it.

The soil erosion rate that this study traced using beryllium-7 showed the primary distribution of soil erosion.

The erosion rate of the 6° gradient field ranged from −1015.4 t km^{-2} to 1574.9 t km^{-2}, with an average of 388.1 t km^{-2}; and the erosion rate of the 20° field ranged from −1307.5 t km^{-2} to 1758.0 t km^{-2}, with an average of 778.2 t km^{-2}. Compared to estimated wind erosion rates obtained from plots using linear or exponential fitting (Table 4), the estimated erosion rates of both fields were greater than the measured values (Table 8). Estimated results were acceptable since there was no significant difference between measured and estimated values ($P > 0.05$). The differences were mainly due to the variation of surface conditions in upwind areas. Bare ground comprised the upwind position of the plots, while grassland with artificial shrubs covered the ground surface for upwind area of the fields. Vegetation decreased ground erodibility below its border, and sheltered the bare field by decreasing erosion energy. Typically, the field length along the wind direction significantly influences wind erosion rates. When the field length is less than the wind fetch length, wind erosion sharply increases with an increase in downwind distances (Zhang et al., 2017). For bare farmland, the wind fetch length could extend hundreds of meters (Zhang et al., 2017; Zobeck et al., 2003). For this reason, measured wind erosion rates should be greater than estimated erosion rates obtained from equations based on plots. Thus, the fact that measured erosion rates were less than estimated erosion rates implied that the vegetation within the upwind position of the observation field affected wind erosion rates more severely than downwind distances.

5. Conclusions

Beryllium-7 measurements provide a quantitative schematic of soil-wind erosion distribution under dual conditions of soil-wind erosion

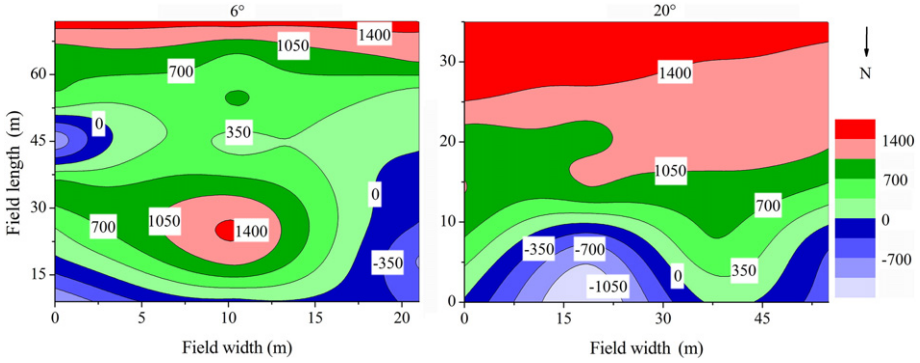

Fig. 9. Isolines of wind erosion rates using beryllium-7 measurements for windward sloping fields. (This study conducted the sampling of the 6° gradient field in 2016 and the sampling of the 20° gradient field in 2015).

Table 8
Estimated wind erosion rates for sloping fields derived from measurements and equations.

Field gradients	Measured erosion rates (t km^{-2})	Equation estimated erosion rates (t km^{-2})					
		2015		2016		Averages	
		Linear	Exponent	Linear	Exponent	Linear	Exponent
6°	388.1	–	–	473.3	445.0	404.7	369.9
20°	778.2	646.9	679.3	–	–	716.7	724.4

and staggered water erosion. For the silt loam sloping fields investigated in this study, both erosion and deposition occurred on the windward slope of cropland on both plot and field scales. Wind-driven soil erosion was linearly or exponentially related to the slope gradient, and the better fitting of linear functions. However, this study determined that approximately 20° was a turning gradient. The increasing rate of soil erosion decreased when the slope gradient was greater than 20°. The direction and shape of soil-wind erosion isolines not only revealed the spatial distribution of erosion rates but also indicated the resultant effective erosion wind direction and the variation of the surface microrelief. The local resultant effective erosion wind direction was from the north during the experimental period of this study. Moreover, convex and concave reliefs of the ground surface generated high or low erosion centers. Although this study developed linear or exponential functions between wind erosion rates and slope gradients based on beryllium-7 measurements, it was difficult to affirm some constants in the equations. Therefore, further research is necessary to develop the equations so that they can be universally applied to wind-water erosion crisscross regions.

Supplementary data to this article can be found online at https://doi.org/10.1016/j.scitotenv.2017.09.238.

Acknowledgements

This study was financially supported by the National Natural Science Foundation of China (Grant No. 41401314), the West Light Foundation of the Chinese Academy of Sciences, the Natural Science Foundation Research Project of Shanxi Province (2015JQ4115), the National Key Research and Development Program of Ministry of Science and Technology (2016YFC0402406), and the Doctoral Scientific Research Fund of the Research Center of Soil and Water Conservation and Ecological Environment, Chinese Academy of Sciences and the Ministry of Education.

References

Al-Amin, N.K.N., Stigter, C.J., Mohammed, A.E., 2010. Wind reduction patterns around isolated biomass for wind-erosion control in a desertified area of Central Sudan. Res. J. Environ. Earth Sci. 2 (4), 226–234.

Atwood-Stone, C., McEwen, A.S., 2013. Avalanche slope angles in low-gravity environments from active Martian sand dunes. Geophys. Res. Lett. 40 (12), 2929–2934.

Ayub, J.J., Lohaiza, F., Velasco, H., Rizzotto, M., Gregorio, D.D., Huck, H.M., 2012. Assessment of ^{7}Be content in precipitation in a South American semi-arid environment. Sci. Total Environ. 441, 111–116.

Beauvais, A., Parisot, J., Savin, C., 2007. Ultramafic rock weathering and slope erosion processes in a South West Pacific tropical environment. Geomorphology 83, 1–13.

Blake, W.H., Walling, D.E., He, Q., 1999. Fallout beryllium-7 as a tracer in soil erosion investigations. Appl. Radiat. Isot. 51, 599–605.

Chaplot, V.A.M., Le Bissonnais, Y., 2003. Runoff features for interrill erosion at different rainfall intensities, slope lengths, and gradients in an agricultural loessial hillslope. Soil Sci. Soc. Am. J. 67, 844–851.

Desmeta, P.J.J., Poesena, J., Goversa, G., Vandaelea, K., 1999. Importance of slope gradient and contributing area for optimal prediction of the initiation and trajectory of ephemeral gullies. Catena 37 (3–4), 377–392.

Du, H.Q., Dou, S.T., Deng, X.H., Xue, X., Wang, T., 2016. Assessment of wind and water erosion risk in the watershed of the Ningxia-Inner Mongolia Reach of the Yellow River, China. Ecol. Indic. 67, 117–131.

Faria, R., Ferreira, A.D., Sismeiro, J.L., Mendes, J.C.F., Sousa, A.C.M., 2011. Wind tunnel and computational study of the stoss slope effect on the aeolian erosion of transverse sand dunes. Aeolian Res. 3, 303–314.

Folk, R.L., Ward, W.C., 1957. Brazos River bar, a study in the significance of grain-size parameters. J. Sediment. Petrol. 27 (1), 3–26.

Fryrear, D.W., Saleh, A., Bilbro, J.D., Schomberg, H.M., Stout, J.E., Zobeck, T.M., 1998. Revised Wind Erosion Equation Technical Bulletin No. 1. US Department of Agriculture-Agricultural Research Service, Wind Erosion and Water Conservation Research Unit, Big Spring, Texas, USA.

Fu, B.J., Liu, Y., Lü, Y.H., He, C.S., Zeng, Y., Wu, B.F., 2011a. Assessing the soil erosion control service of ecosystems change in the Loess Plateau of China. Ecol. Complex. 8, 284–293.

Fu, S., Liu, B., Liu, H., Xu, L., 2011b. The effect of slope on interrill erosion at short slopes. Catena 84 (1–2), 29–34.

Hagen, L.J., Van Pelt, S., Sharratt, B., 2010. Estimating the saltation and suspension components from field wind erosion. Aeolian Res. 1 (3-4), 147–153.

He, J.J., Cai, Q.G., Cao, W.Q., 2013. Wind tunnel study of multiple factors affecting wind erosion from cropland in Agro-pastoral area of Inner Mongolia, China. J. Mt. Sci. 10, 68–74.

Hong, S.W., Lee, I.B., Seo, I.H., Kwon, K.S., Kim, T.W., Son, Y.H., Kim, M.Y., 2014. Measurement and prediction of soil erosion in dry field using portable wind erosion tunnel. Biosyst. Eng. 118, 68–82.

Iversen, J.D., Rasmussen, K.R., 1999. The effect of wind speed and bed slope on sand transport. Sedimentology 46 (4), 723–731.

Landis, J.D., Renshaw, C.E., Kaste, J.M., 2016. Beryllium-7 and lead-210 chronometry of modern soil processes: The Linked Radionuclide aCcumulation model, LRC. Geochim. Cosmochim. Acta 180, 109–125.

Larney, F.J., Bullock, M.S., Janzen, H.H., Ellert, B.H., Olson, E.C.S., 1998. Wind erosion effects on nutrient redistribution and soil productivity. J. Soil Water Conserv. 53, 133–140.

Lee, J., Benson, V.W., Phillips, D.L., 1999. Soil erosion and climate change: assessing potential impacts and adaptation practices. J. Soil Water Conserv. 54 (3), 529–536.

Leenders, J.K., Sterk, G., Van Boxel, J.H., 2011. Modelling wind-blown sediment transport around single vegetation elements. Earth Surf. Process. Landf. 36 (9), 1218–1229.

Liu, J.H., Wang, G.Q., Li, H.H., Gong, J.G., Han, J.Y., 2013. Water and sediment evolution in areas with high and coarse sediment yield of the Loess Plateau. Int. J. Sediment Res. 28 (4), 448–457.
Mahmoodabadi, M., Sajjadi, S.A., 2016. Effects of rain intensity, slope gradient and particle size distribution on the relative contributions of splash and wash loads to rain-induced erosion. Geomorphology 253, 159–167.
Mahmoodabadi, M., Ghadiri, H., Rose, C., 2014. Evaluation of GUEST and WEPP with a new approach for the determination of sediment transport capacity. J. Hydrol. 513, 413–421.
Offer, Z.Y., Goossens, D., 1995. Wind tunnel experiments and field measurements of aeolian dust deposition on conical hills. Geomorphology 14 (1), 43–56.
Ouchi, S., 2015. Experimental landform development by rainfall erosion with uplift at various rates. Geomorphology 238, 68–77.
Owens, P.N., Walling, D.E., He, Q.P., 1996. The behaviour of bomb-derived caesium-137 fallout in catchment soils. J. Environ. Radioact. 32 (3), 191–1996.
Rahmati, O., Tahmasebipour, N., Haghizadeh, A., Pourghasemi, H.R., Feizizadeh, B., 2017. Evaluating the influence of geo-environmental factors on gully erosion in a semi-arid region of Iran: An integrated framework. Sci. Total Environ. 579, 913–927.
Ribolzi, O., Patin, J., Bresson, L.M., Latsachack, K.O., Mouche, E., Sengtaheuanghoung, O., Silvera, N., Thiébaux, J.P., Valentin, C., 2011. Impact of slope gradient on soil surface features and in filtration on steep slopes in northern Laos. Geomorphology 127, 53–63.
Shen, H.O., Zheng, F.L., Wen, L.L., Han, Y., Hu, W., 2016. Impacts of rainfall intensity and slope gradient on rill erosion processes at loessial hillslope. Soil Tillage Res. 155, 429–436.
Sun, W.H., Huang, N., 2017. Influence of slope gradient on the behavior of saltating sand particles in a wind tunnel. Catena 148, 145–152.
Tang, K.L., Hou, Q.C., Wang, K.B., Zhang, P.C., 1993. The environment background and administration way of wind-water erosion crisscross region and Shenmu experimental area on the Loess Plateau. Memoir of Institute of Soil and Water Conservation. 18. Chinese Academy of Sciences and Ministry of Water Resources, pp. 2–15 (in Chinese with English abstract).
Tuo, D.F., Xu, M.X., Gao, L.Q., Zhang, S., Liu, S.H., 2016. Changed surface roughness by wind erosion accelerates water erosion. J soils Sediments 16, 105–114.
USDA, 1951. United States Department of Agriculture (USDA) soil survey mannual. US Department Agriculture Handbook. 18. USA, Washington DC.
USDA, 1996. Wind Erosion Prediction System (WEPS) technical documentation. US Department of Agriculture-Agricultural Research Service. Wind Erosion Research Unit, Manhattan, Kansas, USA.
Vigiak, O., Malago, A., Bouraoui, F., Vanmaercke, M., Poesen, J., 2015. Adapting SWAT hillslope erosion model to predict sediment concentrations and yields in large Basins. Sci. Total Environ. 538, 855–875.
Wallbrink, P.J., Muruay, A.S., 1996. Distribution and Variability of Be-7 in soils under different surface cover conditions and its potential for describing soil redistribution processes. Water Resour. Res. 1 32 (2), 467–476.
Walling, D.E., He, Q., Blake, W., 1999. Use of ^{7}Be and ^{137}Cs measurements to document short- and medium-term rates of water-induced soil erosion on agricultural land. Water Resour. Res. 35, 3865–3874.
Wang, X.B., Oenema, O., Hoogmoed, W.B., Perdik, U.D., Cai, D.X., 2006. Dust storm erosion and its impact on soil carbon and nitrogen losses in northern China. Catena 66, 221–227.
Wang, H.J., Yang, Z.S., Saito, Y., Liu, J.P., Sun, X.X., Wang, Y., 2007. Stepwise decreases of the Huanghe (Yellow River) sediment load (1950–2005): Impacts of climate change and human activities. Glob. Planet. Chang. 57, 331–354.
Wang, S., Fu, B.J., Piao, S.L., Lü, Y.H., Ciais, P., Feng, X.M., Wang, Y.F., 2016. Reduced sediment transport in the Yellow River due to anthropogenic changes. Nat. Geosci. 9 (1), 38–41.
Warren, A., 2007. Sustainability: a view from the wind-eroded field. J. Environ. Sci. 19, 470–474.
Wu, S.Y., 2013. The analysis of variation of weather of Shenmu county in the past 55 years. Climate Shaanxi. 2, pp. 20–23 (in Chinese).
Wu, B., Wang, Z.L., Shen, N., Wang, S., 2016. Modelling sediment transport capacity of rill flow for loess sediments on steep slopes. Catena 147, 453–462.
Yang, M.Y., Walling, D.E., Tian, J.L., Liu, P.L., 2006. Partitioning the contributions of sheet and rill erosion using beryllium-7 and cesium-137. Soil Sci. Soc. Am. J. 70, 1579–1590.
Yang, M.Y., Walling, D.E., Sun, X.J., Zhang, F.B., Zhang, B., 2013. A wind tunnel experiment to explore the feasibility of using beryllium-7 measurements to estimate soil loss by wind erosion. Geochim. Cosmochim. Acta 114, 81–93.
Zha, X., Tang, K.L., 2000. Study on comprehensive control medol of small watershed ecoenvironment in water and wind crisscross zone. J. Nat. Resour. 15 (1), 97–100 (in Chinese with English abstract).
Zhang, P.C., 1997. Spatial and temporal variability of erosion by water and wind in water-wind erosion crisscross region-a case study of Liudaogou watetshed in Jin-Shaan-Meng contiguous areas. Institute of Soil and Water Conservation. Chinese academy of sciences and Ministry of water resources (in Chinese with English abstract).
Zhang, F.B., Yang, M.Y., Zhang, B., 2011. Beryllium-7 activity concentration in plants on the Loess Plateau, China. J. Radioanal. Nucl. Chem. 289, 353–359.
Zhang, F.B., Zhang, B., Yang, M.Y., 2013. Beryllium-7 atmospheric deposition and soil inventory on the northern Loess Plateau of China. Atmos. Environ. 77, 178–184.
Zhang, F.B., Yang, M.Y., Walling, D.E., Zhang, B., 2014. Using ^{7}Be measurements to estimate the relative contributions of interrill and rill erosion. Geomorphology 206, 392–402.
Zhang, Q.Y., Fan, J., Zhang, X.P., 2016. Effects of simulated wind followed by rain on runoff and sediment yield from a sandy loessial soil with rills. J. Soils Sediments 16, 2306–2315.
Zhang, J.Q., Zhang, C.L., Chang, C.P., Wang, R.D., Liu, G., 2017. Comparison of wind erosion based on measurements and SWEEPsimulation: A case study in Kangbao County, Hebei Province, China. Soil Tillage Res. 165, 169–180.
Zhao, C.H., Gao, J.E., Huang, Y.F., Wang, G.Q., Xu, Z., 2017. The contribution of *astragallus adsurgens* roots and canopy to water erosion control in the water-wind crisscross erosion region of the Loess Platreau, China. Land Degrad. Dev. 28, 265–273.
Zhou, Y., Guo, B., Wang, S.X., Tao, H.P., 2015. An estimation method of soil wind erosion in inner Mongolia of China based on geographic information system and remote sensing. J. Arid. Land 7 (3), 304–317.
Zobeck, T.M., Sterk, G., Funk, R., Rajot, J.L., Stout, J.E., Van Pelt, R.S., 2003. Measurement and data analysis methods for field-scale wind erosion studies and model validation. Earth Surf. Process. Landf. 28 (11), 1163–1188.